Journal of Advanced Joining Processes 13 (2026) 100396

Contents lists available at ScienceDirect

Journal of Advanced Joining Processes

journal homepage: www.sciencedirect.com/journal/journal-of-advanced-joining-processes

Depth monitoring protocol for OCT in laser welding with single-mode core and ring beam configurations

Serge André Dib *, Ali Gökhan Demir

Department of Mechanical Engineering, Politecnico di Milano, Via La Masa 1, 20156 Milan, Italy

ARTICLE INFO

Keywords:
Optical coherence tomography
Electric mobility
Online monitoring
Beam shaping

ABSTRACT

Demand for precise monitoring of high-speed laser welding depth is increasing due to growing electric mobility applications. Optical coherence tomography (OCT) can monitor keyhole depth in real time. Newer fiber laser generations, ideal for such applications, offer single-mode core/ring configurations. However, use of OCT with small keyhole apertures may cause measurement inconsistencies. This work proposes a systematic analysis of signal behavior using a contemporary fiber laser with a novel single-mode core and a ring with separate power control, producing focal core and ring sizes of 40 μm and 285 μm, respectively. Bead-on-plate experiments were conducted on 5 mm thick EN AW-1050 Al-alloy. Core and ring power levels were systematically analyzed along with scan speeds. The OCT beam of 34 μm was aligned with the laser beam using different laser process parameters. Keyhole depth was compared to seam depth from metallographic cross-sections. The study involved systematic development of an alignment protocol to highlight the sensitivity of OCT measurements. The results revealed that a fine alignment of the OCT beam with respect to the laser beam is crucial for reliable acquisitions. The procedure was able to monitor keyhole depths for weld speeds of up to 800 mm/s using only the single-mode beam.

Introduction

Reducing CO_2 emissions involves a transition in the automotive industry to different, particularly renewable energy sources. In order to reach this goal, a significant increase in the share of electric vehicles and hybrid cars is required. By 2025, an electrified powertrain is expected to be implemented by one in four cars worldwide (Demir et al., 2024). Growing attention to the importance of electromobility highlights the need for highly digitalized, adaptable, and robotized manufacturing technologies. Accordingly, laser-based applications come as an essential solution. Remote laser welding, being a promising joining technology with high precision, well-defined heat input, and deep penetration has attracted significant attention in the academic and industrial sectors. Remote laser welding has become a fundamental tool for large-scale production, especially due to its flexibility in terms of automation. Particularly, laser beam welding (LBW) is widespread in the e-mobility sector, spanning several applications, including battery electrodes, battery packs, and stator hairpins.

However, despite these advantages, conventional laser beam distributions consisting of a Gaussian profile often exhibit possible drawbacks for laser material processing. Its high power distribution density is believed to cause considerable thermal gradient and defects (Galbusera et al., 2024). To overcome such challenges, spatial beam shaping prevails as a solution, tailoring the energy input and modifying the given thermal field. Among the most addressed dynamic beam shaping technologies in industrial applications, contemporary laser solutions providing core/ring beam profiles emerge as one of the most prevalent (Mohammadzadeh Sanandaji et al., 2025; Sokolov et al., 2021). The added ring-shaped beam, coaxially surrounding the core, allows controlling the heating and cooling rates in and around the melt pool, as well as contributing to an enlargement in the keyhole section (Wang et al., 2020; Haeusler et al., 2018).

As these beam shaping technologies are implemented to ensure process stability, reliably monitoring the laser weld depth and its consistency emerge as a fundamental aspect on an industrial scale (Spurk et al., 2024). Numerous methods have been proposed to monitor the weld depth, namely visual imaging, acoustic signals, and indirect observation through optical radiation (Xie et al., 2023). In recent years, optical coherence tomography (OCT) emerges as a robust choice, offering to measure the weld depth in real-time. In laser deep penetration

* Corresponding author.
E-mail address: serge.dib@polimi.it (S.A. Dib).

https://doi.org/10.1016/j.jajp.2026.100396

Available online 28 March 2026

welding, the OCT beam is deployed co-axially to the laser processing beam (Webster et al., 2010). When the OCT beam is aligned properly towards the keyhole's bottom, the technology provides fast and direct measurement of the keyhole depth. Generally, the keyhole depth is typically insignificantly lower than the weld depth (Mittelstädt et al., 2019; Blug et al., 2011). In consequence, the keyhole depth can be considered as a direct indicator of the weld depth in OCT in-situ monitoring applications.

As keyhole fluctuations and instabilities can potentially affect the OCT acquisitions (Boley et al., 2013), the quality of the OCT online depth measurement depends intrinsically on the welding conditions and hence the employed laser process parameters (Schmoeller et al., 2022). Typically, the deepest point of the keyhole trails 0–0.04 mm behind the laser beam. This trailing establishes the lag distance that is associated to the OCT beam positioning with respect to laser beam (Dupriez and Denkl, 2017). The spatial and temporal positioning and maintaining of the OCT measurement beam which points towards the deepest point of the keyhole is considered as a challenging task (Boley et al., 2019). Several process parameters such as the laser power, the weld speed, and the material-dependent thermal conductivity have a direct influence on the keyhole shape, tilt, and volume. Process disturbances and unstable capillary might render the OCT sensor signals unreliable and eventually causing signal fluctuations and measurement errors (Dorsch et al., 2019). Therefore, a proper alignment of the OCT beam within the keyhole and towards the keyhole's deepest point is necessary. The applicability of OCT measurements in LBW often necessitates wider keyhole openings as a means to allow broader reach of the OCT beam to the bottom of the keyhole with minimal obstacles along the optical path. In general, relatively lower weld speeds (<100 mm/s) are employed, allowing a reasonable estimation of the weld depth with temporal sampling frequencies in the range of 100 kHz. On the other hand, accurate calibration procedures are required to exploit the measurement system correctly with the available sampling frequencies.

OCT in-situ monitoring of the keyhole depth in literature is often based on high power levels, i.e. from 2 to 6 kW, combined with low weld speeds ranging from 10 to 200 mm/s. This combination of laser process parameters eventually yields an enlarged keyhole shape, rendering the OCT beam alignment relatively simpler. Moreover, use of OCT during welding using a single-mode beam has been studied only to a limited extent due to difficulty in aligning the beam spatially and temporally in a small capillary aperture (Schmoeller et al., 2019; He et al., 2024). In remote laser welding of battery tab connectors, a contemporary core and ring beams configuration has been studied (Sokolov et al., 2021). Thin foil stacks of Al-Cu, with a few hundred micrometers of thickness, were welded using an adjustable ring-mode laser. The study investigated the variation effects of the core and ring powers—using core power levels between 650 and 800 W and ring power levels between 50 and 1500 W at a weld speed of 175 mm/s. With the addition of the ring profile, the keyhole resulted in a more stable and larger volume. The OCT measurement error of the weld penetration depth was reduced significantly when compared to the same measurements for which only the core beam was adopted. In addition, in-situ keyhole monitoring using a highly brilliant, single-mode beam with a spot diameter of 55 μm, has been reported in the literature (Schmoeller et al., 2019) using power levels between 1.5 and 2.7 kW and a weld speed of 165 mm/s. The results showed a high dependency of the OCT signal quality on the different process parameters. Notable differences between the real weld depth and the measured weld depth were seen when aiming for deeper welds with the single-mode core beam. In general, a small laser beam diameter and a low penetration depth complicate a steady and precise measurement of the keyhole (Hollatz et al., 2020).

The importance of the calibration of the OCT beam position is apparent for industrial applications, as well as a greater understanding of the process dynamics (Dupriez and Denkl, 2017). Moreover, for measuring the keyhole depth through small keyhole apertures at high scan speeds, such procedures are crucial for reliable and meaningful measurements. As a matter of fact, correct beam alignment procedures are crucially important to fully exploiting the potential of this technology when adopted in electric mobility applications (Dorsch et al., 2019; Beck et al., 2021). To the authors' knowledge, OCT keyhole depth measurement with single-mode fiber lasers at scan speeds of several hundreds of mm/s has not been previously reported in literature. In this work, the influencing factors on OCT measurement signals were investigated for a robust and reliable process monitoring in remote laser welding. Bead-on-plate experiments were conducted using a fiber laser with single-mode core and ring configuration on Al-alloy samples. The feasibility of using OCT to measure small capillary depths at relatively high scan speeds was assessed. OCT beam alignment procedures were presented to show the sensitivity of the process during welding with speeds of up to 800 mm/s without and with added ring power that is often used as aid to enhance measurement capability. The measurements were compared to melt track depths made on metallurgical cross-sections to assess the influence of the alignment procedure.

Experimental setup

Laser source and scanner

Fig. 1 a displays a schematic of the experimental setup used in this study. A NIR laser source with adjustable-mode beam and a wavelength of 1070 nm was used (YLS-2000/4000-SM-AMB, IPG Photonics, Cambridge, CA, USA). The laser system was characterized by a single-mode beam with a fiber core diameter of 14 μm, complemented with a ring beam with a fiber core inner diameter of 40 μm and a fiber core outer diameter of 100 μm. The beam was focused using a 140 mm collimating lens and a 400 mm focusing lens. A separate control of the power content within the single-mode and the ring portions of the beam was possible. The resulting focal diameters were 40 μm for the core beam, and 115 μm and 285 μm for the inner and outer ring beams, respectively (see Fig. 1 b and c). Those values were further confirmed using a beam profiler (SP90609 BeamPeek, Ophir Optronics Solutions, Massachusetts, USA). The movement of the process beam relative to the sample surface was done by using a galvanometric scanner head (2D High Power Scanner D33, IPG Photonics, Cambridge, CA, USA). Table 1 portrays all related properties of the used laser system.

OCT system

An optical coherence tomography system (LDD-700, IPG Photonics, Cambridge, CA, USA) was used to monitor the weld process and measure the in-situ keyhole depth variation. The superluminescent diode (SLD) broad-band wavelength was between 800 and 900 nm. The depth measurement system uses the inline coherent imaging technique, which is related to OCT and low-coherence imaging methodologies. The OCT beam is directed coaxially through the same lens optics as the process beam, and onto the top surface of the material (see Fig. 1), where it gets reflected and re-enters the system, and into the OCT detector. The measurement is done at sampling rates of up to 250 kHz. The focal diameter of the OCT measuring beam was equal to ~ 34 μm, thus slightly smaller than the focal diameter of the single-mode core beam. A detailed description of the alignment protocol is described in section "Influence of process parameters on weld width and depth". Table 2 shows the properties of the OCT system used in this study.

Material

The material used in this study was chosen as EN AW 1050 Al-alloy due to its lightweight, which plays a fundamental role in the automotive sector, particularly in e-mobility applications used as material for battery busbars, module cases, as well as cooling plates (Köhler et al., 2019). The chemical composition of the material used is shown in Table 3. The specimens were 5 mm thick. Bead-on plate weld seams with

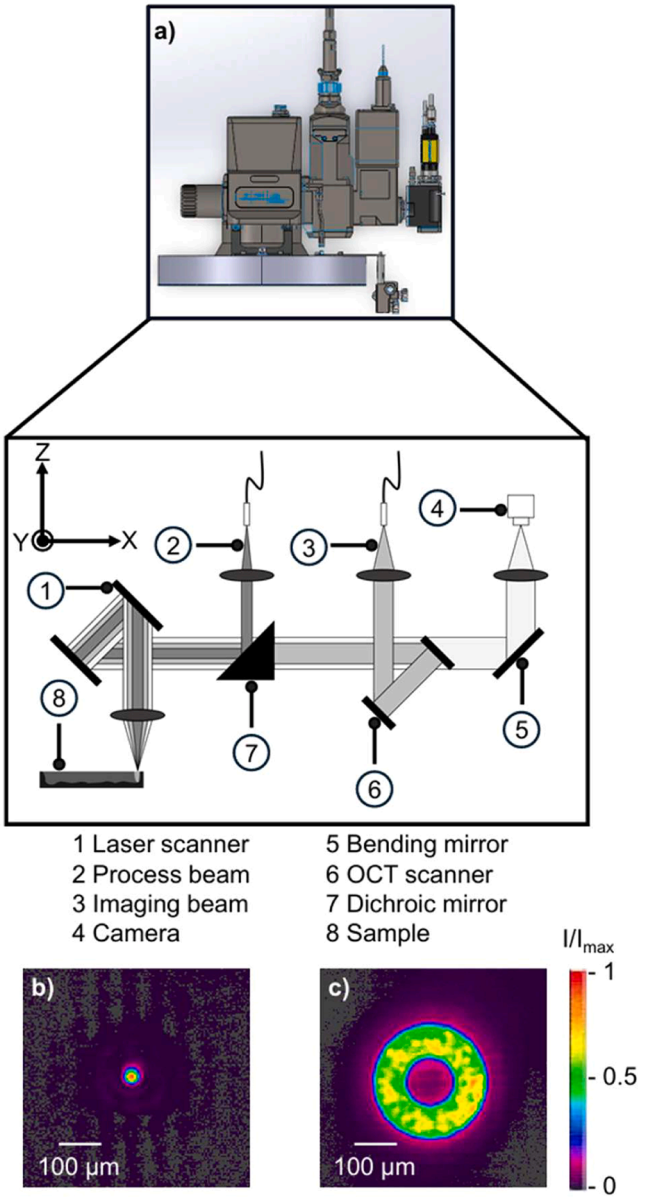

Fig. 1. a) Schematic of the experimental setup used for this study. Beam profiles for b) the single-mode beam and c) the ring beam. The intensity of the beam profiles I is normalized with the maximum intensity I_{max}.

a weld length of 20 mm were produced. No shielding gas was applied. The surface of these specimens was cleaned from possible contaminants using acetone and alcohol.

Characterization equipment

Cross-sectional samples were taken from the welded specimens. SiC paper up to 2500 grits was used to ground the samples (Maurya et al., 2024). 6 µm, 3 µm, and 1 µm diamond pastes were utilized, respectively, for the polishing process. Chemical etching was done to reveal the welded regions in the cross-sections. Keller's reagent (95% H2O + 2.5% HNO3 + 1.5% HCl + 1.0% HF) was utilized as the chemical etchant. As a final step, the etched samples were analyzed using optical microscopy (Quick Vision Pro, Mitutoyo Corporation, Kawasaki, Japan). Fig. 2 a shows a schematic of the measurements for the cross-sections of the weld seam. For each joint condition, the experimental weld depth (h) was taken as the main indicator. In addition, and generally, weld depths obtained from metallographic cross-sections are prone to error. For this reason, for each specimen, three cut sections were obtained at approximately one-quarter, two-quarters, and three-quarters of the total weld length (L_{Weld}) of the bead, see Fig. 2 b. The weld depth was measured once within each of the cross-sections. This approach provided an estimate of measurement variability, validated by reporting a consequent mean and standard deviation.

Table 1
Main properties of the laser system.

Parameter	Specification
Brand and model	IPG YLS-2000/4000-SM-AMB
Maximum core power [kW]	2
Maximum ring power [kW]	4
Wavelength [nm]	1070
Central fiber core diameter [µm]	14
Ring fiber diameter [µm]	40 (inner), 100 (outer)
Collimating length [mm]	140
Focusing length [mm]	400
Focused core diameter [µm]	40
Focused ring diameter [µm]	115 (inner), 285 (outer)

Table 2
Main properties of the OCT system.

Parameter	Value
Imaging wavelength [nm]	800 to 900
Power [mW]	< 20
Measurement frequency [kHz]	up to 250
Imaging beam diameter [µm]	34

Table 3
Elemental content of EN AW 1050 used (wt%) (Köhler et al., 2019).

Al	Si	Fe	Cu	Mn	Mg	Zn	Ti
≥ 99.5	≥ 0.25	≥ 0.4	≥ 0–05	≥ 0–05	≥ 0.05	≥ 0.07	≥ 0.05

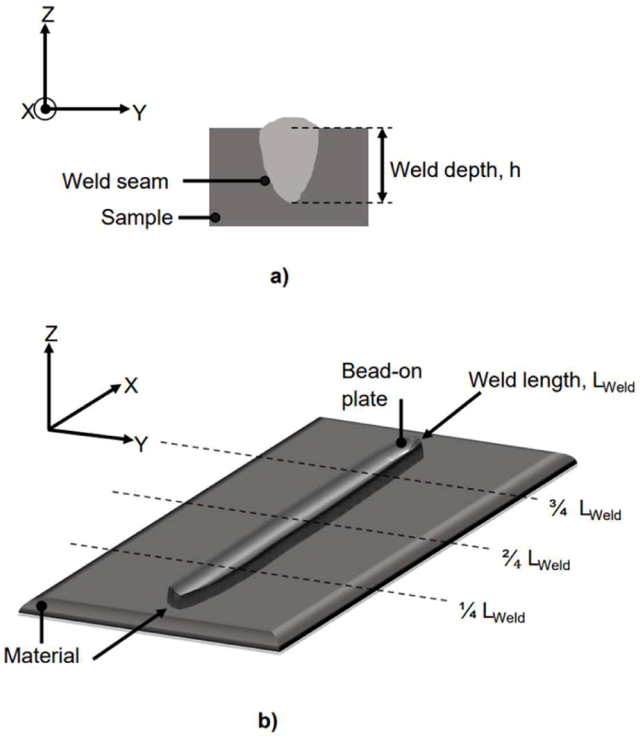

Fig. 2. a) Metallographic cross-section analysis. b) Cut sections applied for each produced weld bead.

Definition of the OCT alignment protocol

Table 4 shows the settings used for the in-situ OCT monitoring of the keyhole depth. A noise threshold of 13 dB was applied for the processing of the in-situ OCT acquisitions. This value was chosen based on prior experimentations and supported by literature where similar threshold values were shown to effectively limit the errors due to background noise (Fleming et al., 2023). Additionally, at the beginning of the weld, the process is in conduction mode, whereas at the end the keyhole might get disturbed and collapse (Hollatz et al., 2020). These phenomena lead directly to a shallower weld depth. Thus, the region of interest excluded the beginning and the end of the 20 mm laser weld length. Typical data resulting from an OCT acquisition is portrayed in Fig. 3 a. The OCT provides the optical path length till the point of light reflection and back onto the detector. This path length can be measured with a resolution of up to 250 kHz. The white points representing the raw data of the returned signal suffer from a level of noise. In order to retrieve the actual keyhole depth, a raw data filter algorithm is applied to track the keyhole's actual depth. This is illustrated in Fig. 3 b.

In general, during the weld process, the keyhole manifests after a rapid melt and evaporation of the metal during laser-material interaction on the surface. Under the effect of steam recoil pressure, the sidewall of the keyhole enlarges outward continuously (Shu et al., 2025). The front of the keyhole constitutes the area to be welded. Whereby, the tail of the keyhole constitutes the molten material. As a result, the tail of the keyhole is subjected to less expansion resistance than that of the front. This concept establishes the foundation for the lagging of the keyhole's deepest point behind the laser beam (Shu et al., 2025). The lag distance is represented by the (x,y) coordinates that are to be obtained for a correct OCT beam alignment.

Fundamentally, the calibration protocol was accomplished employing two software utilities provided by the manufacturer's software, namely the keyhole three-dimensional viewer module, and the real-time keyhole depth monitoring module, herein denoted as 3D Viewer and KDM, respectively. What follows is a step-by-step explanation of the process development for those modules, as a means to obtain the final (x, y) coordinates.

The 3D viewer module is used to reconstruct the keyhole geometry through a sequential of lateral coherent light surface scans. Each scan leads to a 3D pointcloud dataset, based on a pre-defined field of view (FOV) and a pixel resolution. The scanning process is governed by temporal and spatial relationships that link the weld process with the OCT acquisition. The scan time of the OCT beam of the keyhole, t_{scan}, is a function of a spatial resolution–defined by the number of pixels in x and y direction, n_{px} and np_y, respectively–and the maximum sampling frequency of the OCT system, f_{OCT}.

$$t_{scan} = \frac{n_{Px} \cdot n_{Py}}{f_{OCT}} \tag{1}$$

For one complete acquisition cycle, the total scan time is determined by adding t_{scan} to t_{etc}, a term accounting for scanner jumps and initialization of the laser head.

$$t_{OCT} = t_{scan} + t_{etc} \tag{2}$$

The spatial resolution of the 3D keyhole pointcloud is based on the total number of pixels in the coordinate system in x, n_{px}, and in y, n_{py}. The total time for the acquisition cycle is then divided across the scan pattern. The time required to scan a single line along the x coordinate system, Δt_x, is defined as

$$\Delta t_x = \frac{t_{OCT}}{n_{Py}} \tag{3}$$

Similarly, the time defined in the y coordinate system is:

$$\Delta t_y = \frac{t_{OCT}}{n_{Px}} \tag{4}$$

From these scans along the lines, the model derives the temporal resolution per pixel. Consequently, the scan time between one pixel and the consecutive one, for both the x-direction (Δt_{x-x}), and the y-direction (Δt_{y-y}) can be described as follows:

$$\Delta t_{x-x} = \frac{\Delta t_x}{np_x} = \frac{t_{OCT}}{n_{Py} \cdot n_{Px}} = \Delta t_{y-y} \tag{5}$$

Finally, analogous to Eq. (1), the weld time of the laser beam, t_{weld}, can be described by:

$$t_{weld} = \frac{L_{weld}}{v_{weld}} + t_{etc} \tag{6}$$

where L_{weld} is the weld length and v_{weld} is the weld speed.

Fig. 4 a schematizes the coordinate system implemented in model. The governing equations constitute the calibration protocol, a systematic, iterative approach designed to precisely align the OCT beam

Table 4
Settings used for the in-situ OCT monitoring of the keyhole depth.

Parameter	Value
Signal intensity threshold [dB]	13
Region of interest – Left [µm]	1000
Region of interest – Right [µm]	19,000
Correlation method	Close to reference plane within a time span
Correlation time [ms]	2
Weld direction smoothing	Median
Weld direction smoothing window [µm]	2000
Window direction	Symmetric
Intensity [dB]	10–13

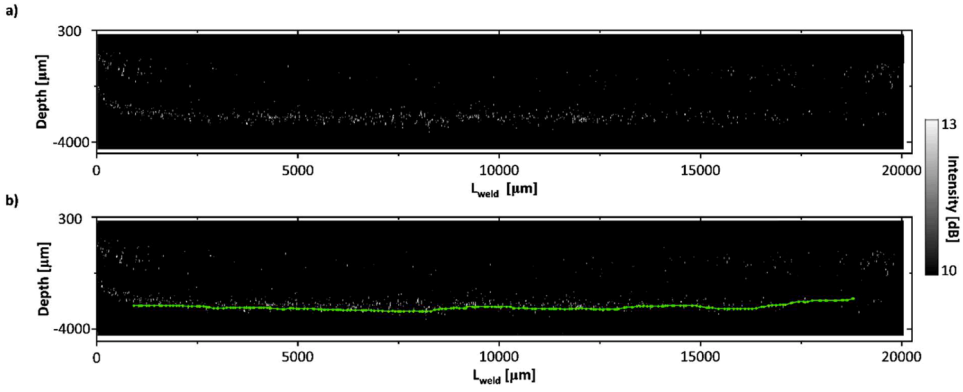

Fig. 3. Acquisition signal example: tracking algorithm a) disactivated and b) activated.

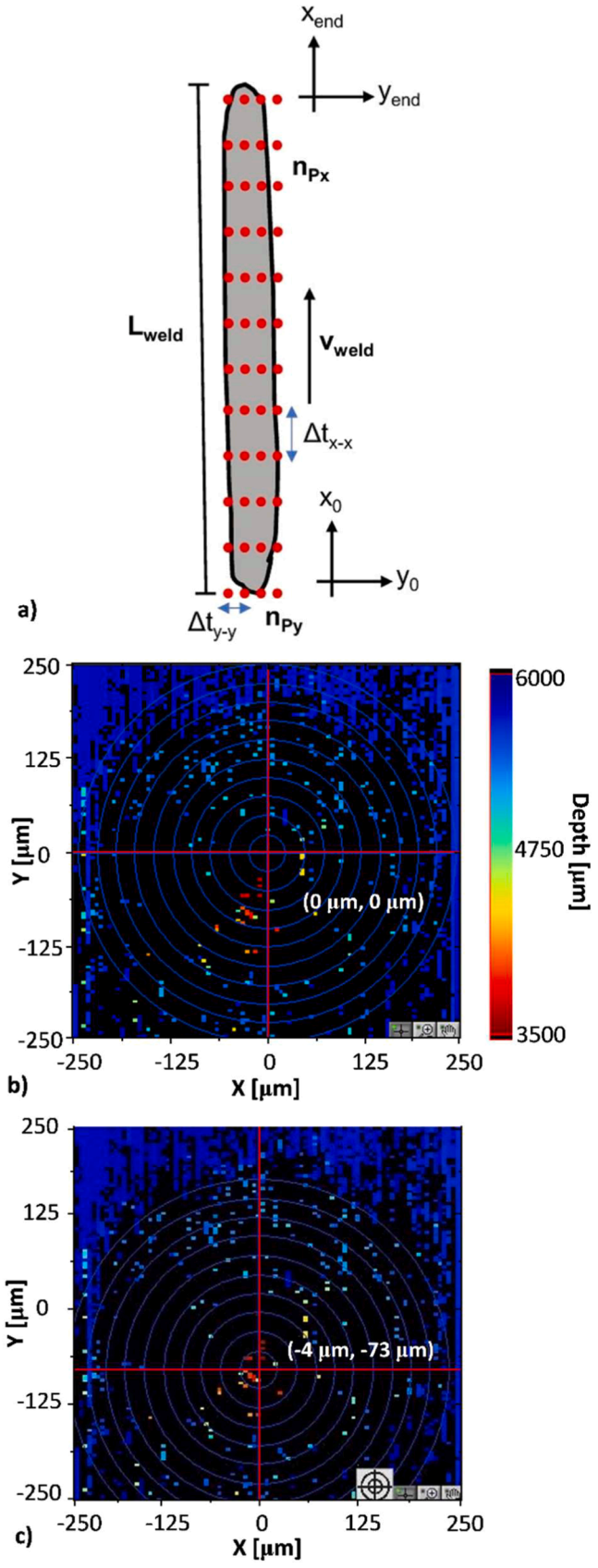

Fig. 4. a) Representation of the in-situ scan process of a weld bead; OCT-laser lag distance adjustment: b) OCT position at the origin, c) OCT position towards the deepest points of the keyhole.

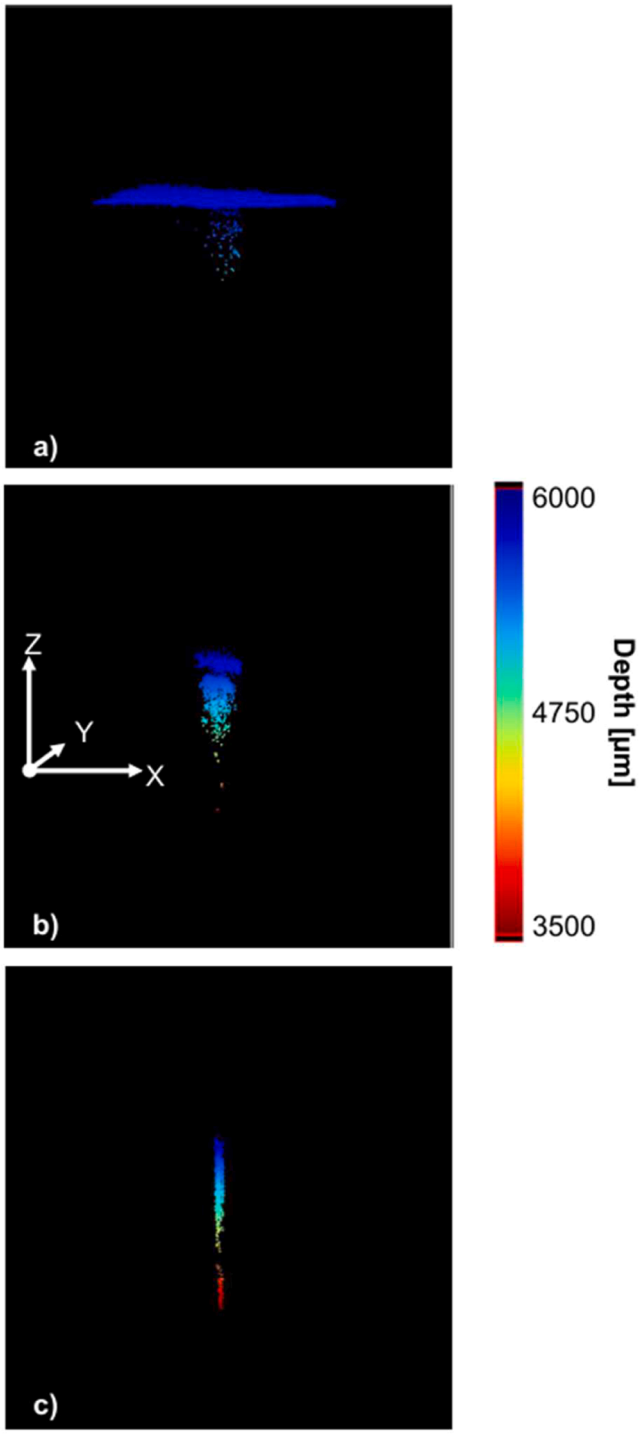

Fig. 5. 3D keyhole pointcloud for different field of view configurations: a) 2000 × 2000 µm, b) 500 × 500 µm, and c) 100 × 100 µm.

exactly in the keyhole's deepest point. This alignment is achieved following a two-stage optimization procedure. First, the spatial lag between the OCT beam and the laser beam is determined. And second, the FOV is continually refined to enhance the lag distance accuracy.

The initial stage, lag distance extraction, starts with a series of surface scanning of the morphology of the keyhole, in real-time during the weld process. The primary goal is to identify the lag distance and iteratively optimize it between one surface scan and the subsequent one. At the beginning of the calibration, and prior to the first surface scan, the OCT beam is typically positioned in the origin at the x–y, i.e. at the (0,0)

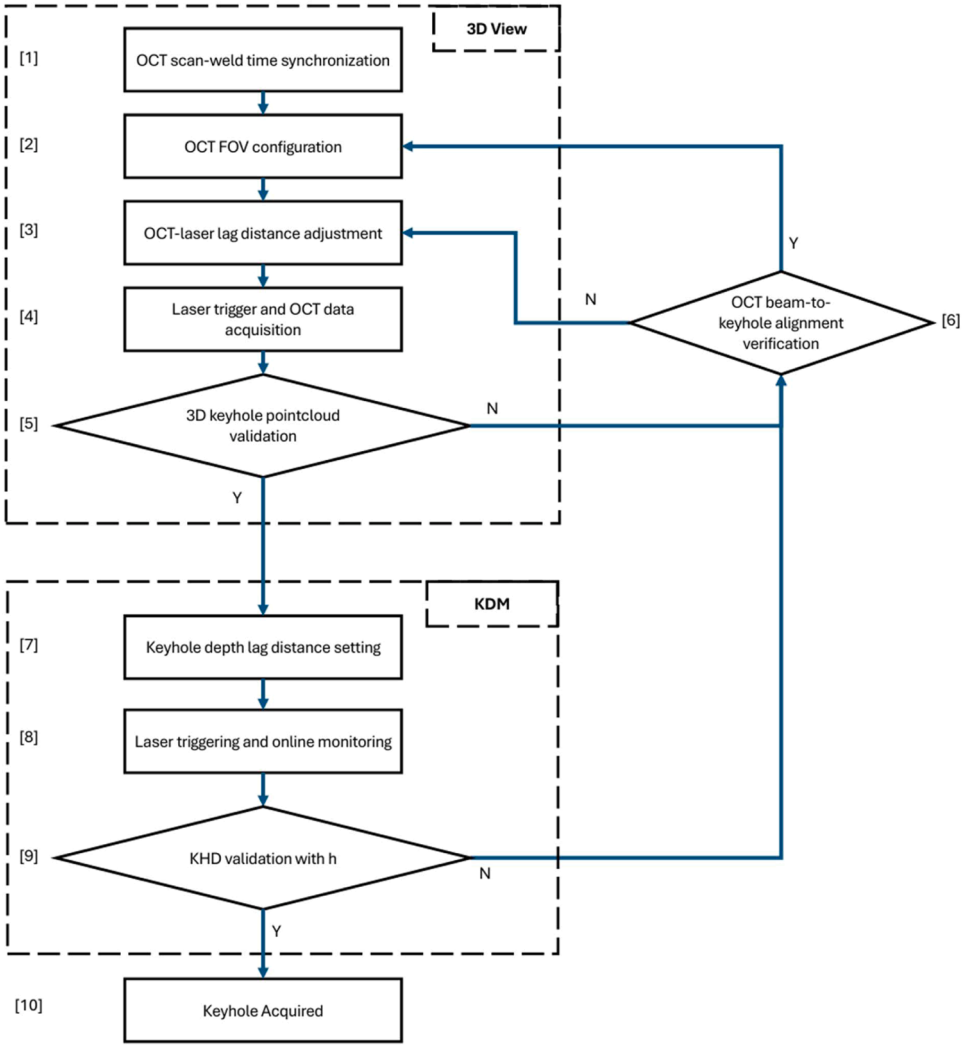

Fig. 6. Iterative process for a fine alignment of the OCT beam within the keyhole.

position. Fig. 4 b shows the x-y depth map of the acquired 3D keyhole after the first surface scan at (0,0). The depth map includes a crosshair that intersects at the pre-chosen (0,0) position. The region corresponding to the deepest point of the keyhole can be identified by the presence of the red dots in the point cloud which represent the maximum depth according to the depth map color scale. The crosshair is then repositioned on this region and the coordinates in x,y directions are consequently extracted (see Fig. 4 c). These coordinates constitute the lag distance of the OCT beam attributed to the consecutive surface scan to be done. These steps are repeated in succeeding surface scans to progressively refine the OCT beam's spatial alignment. Following the initial stage, the second stage of the calibration, FOV refinement, is performed to increase the pixel resolution towards the keyhole's deepest point, since at the beginning, the keyhole is first scanned using a wide FOV with a fixed temporal resolution. This FOV is kept large to assess the correct position of the keyhole. As the FOV is reduced, more data points from the keyhole profile get registered, enhancing the resolution of the internal section of the keyhole. The FOV reduction effect is illustrated Fig. 5. The 3D point cloud in Fig. 5 a exemplifies a result of a surface scan for a 2000 × 2000 μm FOV configuration. Fig. 5 b and c, instead, display the same result of the previous scan surface, with narrower FOVs of 500 × 500 μm and 100 × 100 μm, respectively. By restricting the FOV, the morphological details towards the keyhole's deepest point are enhanced, depicting with greater precision its inner part, thus leading to an optimized lag distance extraction from one scan to the subsequent one. Several iterations are required to achieve a fine calibration quality, during which the lag distance between the OCT and laser beams is continuously adjusted. The more iterations were executed, the minimum the effective distance between the deepest point of the keyhole and the OCT probe beam got. The lag distance extracted in the final surface scan of the keyhole is considered the effective lag distance. Subsequently, this ends the work in the 3D Viewer module, and the lag distance is used for the KDM module, as explained in what follows.

The KDM module exploits the lag distance extracted from the 3D Viewer module to position the OCT beam within the allocated x and y coordinates during the online monitoring process. In this module, the keyhole depth is spatially and temporally monitored along the weld length of the weld, in-situ. The OCT scanning approach changes in that case. As a characteristic feature of the OCT scan in the KDM utility, the beam splitter module in the optical path length of the probe beam divides the light into two measuring beams. The first one is directed towards the keyhole, with the pre-defined x and y coordinates. The second, instead, is directed towards the flat surface of the workpiece, and acts as the zero-plane. The splitting of the measuring beam and its reflections back to the OCT detector allows discrimination between keyhole depth and workpiece surface. Consequently, the keyhole depth per instant is computed from the difference between the distance value of the keyhole and the distance value of the workpiece surface. In addition, the OCT in-situ scan is based on a cycle time, where a major fraction of the time is dedicated to scanning the keyhole–based on the

Table 5
Fixed and variable parameters of the experimental design.

Fixed parameters	
Configuration	Bead-on plate
Defocus Δz [µm]	0
Core spot diameter d_{Core} [µm]	40
Ring spot diameter d_{Ring} [µm]	115 (inner), 285 (outer)
Weld seam length L_{Weld} [mm]	20
Variable parameters	
Core powerP_{Core} [kW]	1, 2
Ring power P_{Ring}	$0{\cdot}P_{Core}$, $1{\cdot}P_{Core}$, $2{\cdot}P_{Core}$
Weld speed v_w [mm/s]	100, 200, 400, 800
Alignment procedure	Rough, fine

pre-defined lag distance, whereby a minor fraction of the time is dedicated to scanning the flat surface. Similarly, the intensity of the two measuring beams is divided between the two scans, with the intention to direct the major intensity into the keyhole. To describe the characteristics of the signal and to estimate the keyhole depth (KHD), the scan yields in a point cloud of distance values distributed spatially along the weld length. KHD is computed as follows:

$$KHD = \frac{1}{k}\sum_{i=1}^{k}(z_i - \bar{z}_i)^2 \tag{7}$$

where k is the number of cycles of the OCT scanning of the workpiece during the weld, z_i is the returned distance of the keyhole depth per cycle, and $\bar{z}_i$ is the returned distance of the flat surface of the workpiece. Further description of the measuring principle can be found in (Schmoeller et al., 2019; Kogel-Hollacher et al., 2016; James and Webster, 2012).

The complete iterative approach based on both the 3D Viewer and the KDM utilities is illustrated in Fig. 6. The procedure begins within the 3D Viewer module, where an initial iterative loop is executed (steps [1] to [6]). This loop involves acquiring a 3D keyhole pointcloud, validating its quality, and verifying the OCT beam-to-keyhole alignment. Based on this validation, both the OCT lag distance and the FOV are progressively refined to improve the spatial resolution of the inner part of the keyhole. This first stage is repeated up until an optimal (x,y) lag distance–corresponding to accurate spatial coordinates of the keyhole's deepest point–is extracted. This final lag distance is transferred to the KDM module. In the second stage (steps [7] to [9]), online monitoring of the keyhole depth is performed implementing the final lag distance obtained from the 3D View module. The resulting KHD is then validated against the experimental weld depth h. If the KHD measurement is inaccurate, it might indicate an erroneous alignment. In that case, the iteration process returns to the alignment verification step [6], beginning a new optimization loop until a reliable and validated KHD acquisition is achieved (step [10]).

Experimental design

Influence of process parameters on weld width and depth

In order to systematically assess the effect of the different laser process parameters on the resulting keyhole and the relative in-situ OCT acquisitions, a parametric design of experiments was conducted. A full-factorial plan was established based on a variation of combinations of laser core power P_{Core}, laser ring power P_{Ring}, and laser weld speed v_w. This laser ring power was set to three levels, with multipliers of the core power at zero, one, and two P_{Core}, maintaining a proportional relationship between the two laser beam powers. The welding study comprised 24 process parameters combinations. The chosen combination of parameters ensured a direct influence on the resulting dynamics of the keyhole (Schmoeller et al., 2020). The combinations included

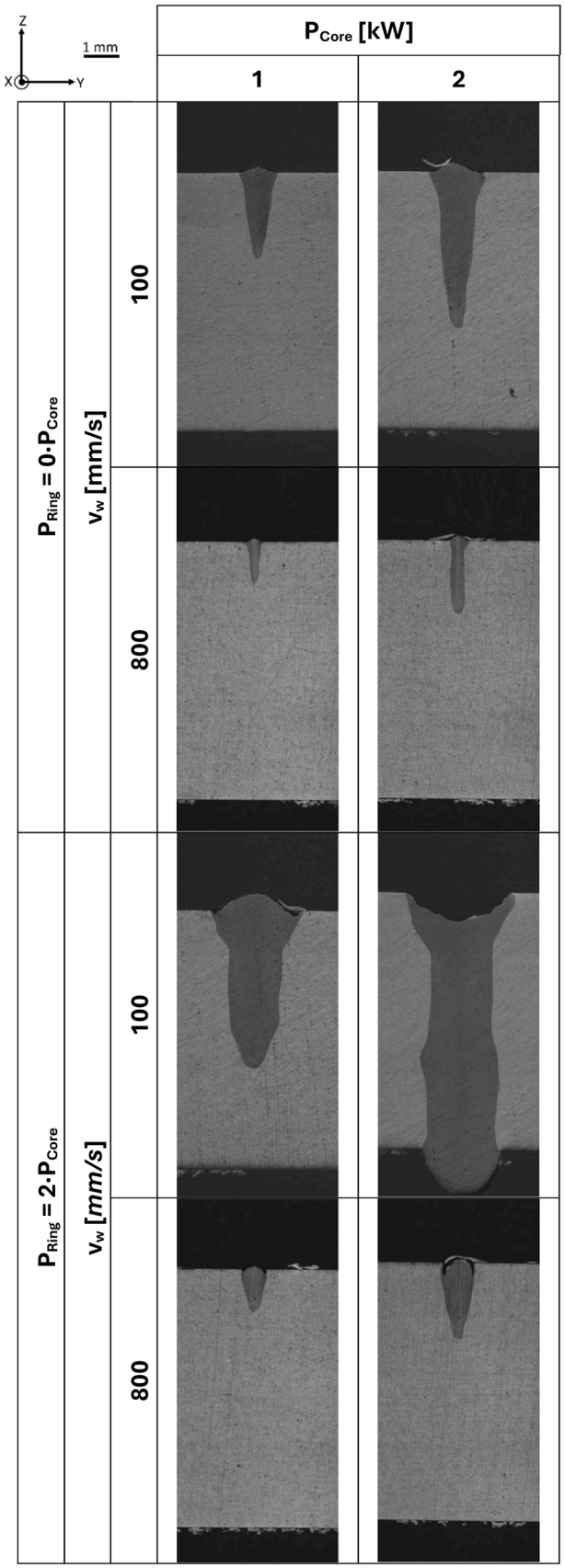

Fig. 7. Influence of the process parameters on the weld seam obtained from the metallographic cross-sections.

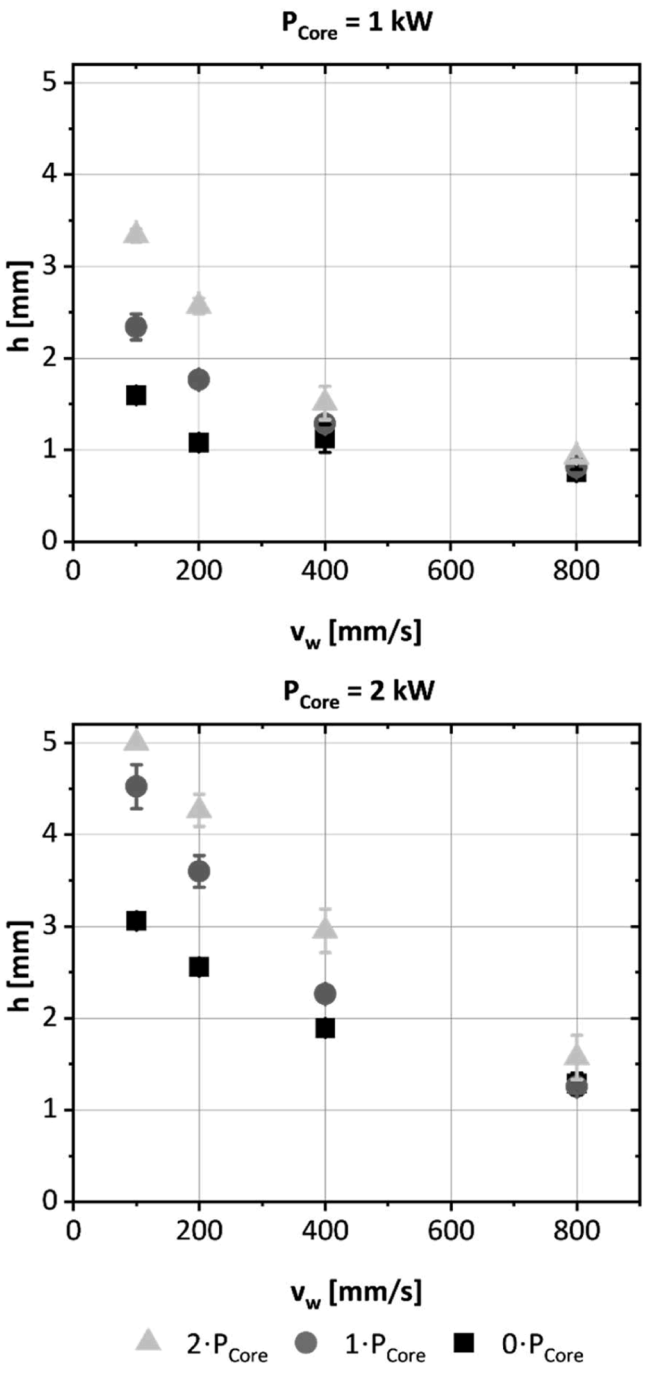

Fig. 8. Influence of the process parameters on the experimental weld depth h.

high weld speeds at 800 mm/s, previously unexplored within OCT measurements, coupled with a single-mode beam. It has been previously shown that the keyhole depth correlates strongly with the weld speed (Huegel and Graf, 2009). Higher weld speeds render the keyhole thinner, thus leading to possible complications in the OCT beam positioning. In contrast, the core beam power is directly correlated to the generation and the depth of the keyhole. Whereby, the ring beam allows a controlled distribution of temperature around the molten pool and enlargement of the keyhole (Galbusera et al., 2024; Sokolov et al., 2021; Wang et al., 2020). Table 5 summarizes the fixed and variable parameters of the experimental design.

Measurement performance of OCT in rough and fine calibration conditions

In the following, two alignment procedures are developed and analyzed, namely a "rough alignment" and a "fine alignment". The main objective was to evaluate the sensitivity and impact of the OCT beam positioning within the keyhole, which might lead to erroneous measurement results in case of misalignment. In the "rough alignment" protocol, the lag distance is deduced after a total of up to three iterations (see the iterative process in Fig. 6). The resulting 3D keyhole morphology was not necessarily validated, and the (x,y) coordinates of the OCT were not necessarily in the vicinity of the deepest point of the keyhole. Yet, following this approach renders the process more time-efficient, relevant for industrial applications where a rapid process setup is prioritized. Nevertheless, this protocol might lack precision in the OCT beam positioning, since the alignment protocol is not performed extensively. Conversely, in the "fine alignment" protocol, the iterative process is carried out up until total validation. No time, cost, or material limitations are considered. The lag distance is optimized and adjusted accordingly after each iteration. This longer process ensures a

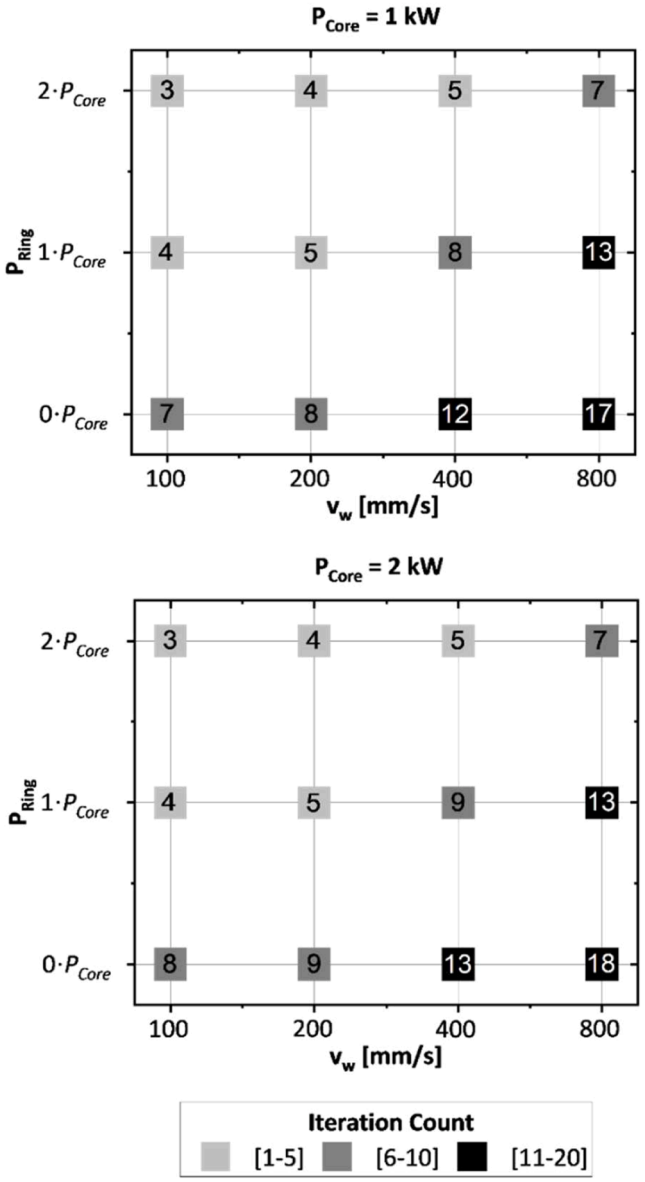

Fig. 9. Influence of the process parameters on the iteration counts for a "fine alignment".

much finer alignment of the OCT beam towards the keyhole's deepest point. In such case, the outcome of the acquisition is expected to be more reliable and accurate, with a possible mitigation of a measurement error that might have resulted otherwise due to beam misalignment. Implementing two distinct protocols for this research work establishes a trade-off between alignment precision and time efficiency. The work systematically examines the stability of the procedure, crucial for reliable acquisitions of the weld depth and quality assurance.

Results

Weld depth measured in metallographic cross-sections

Exemplary cross-sections are shown in Fig. 7. In order to better visualize variations, and for ease of analysis, only the weld seams resulting from the lowest and the highest weld speeds were shown, being 100 mm/s and 800m/s, respectively. The same reasoning was adopted

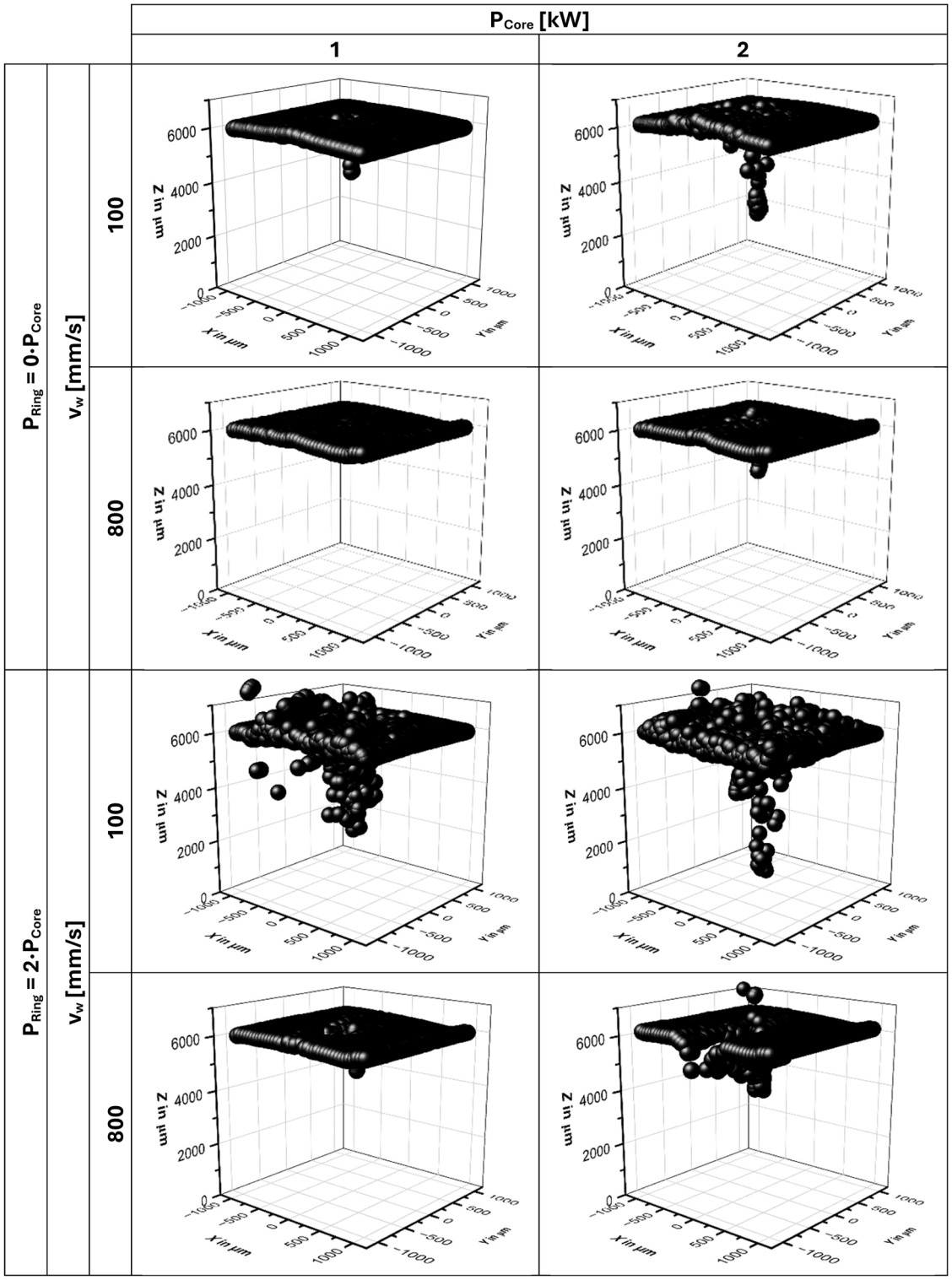

Fig. 10. Influence of the process parameters on the 3D keyhole pointcloud.

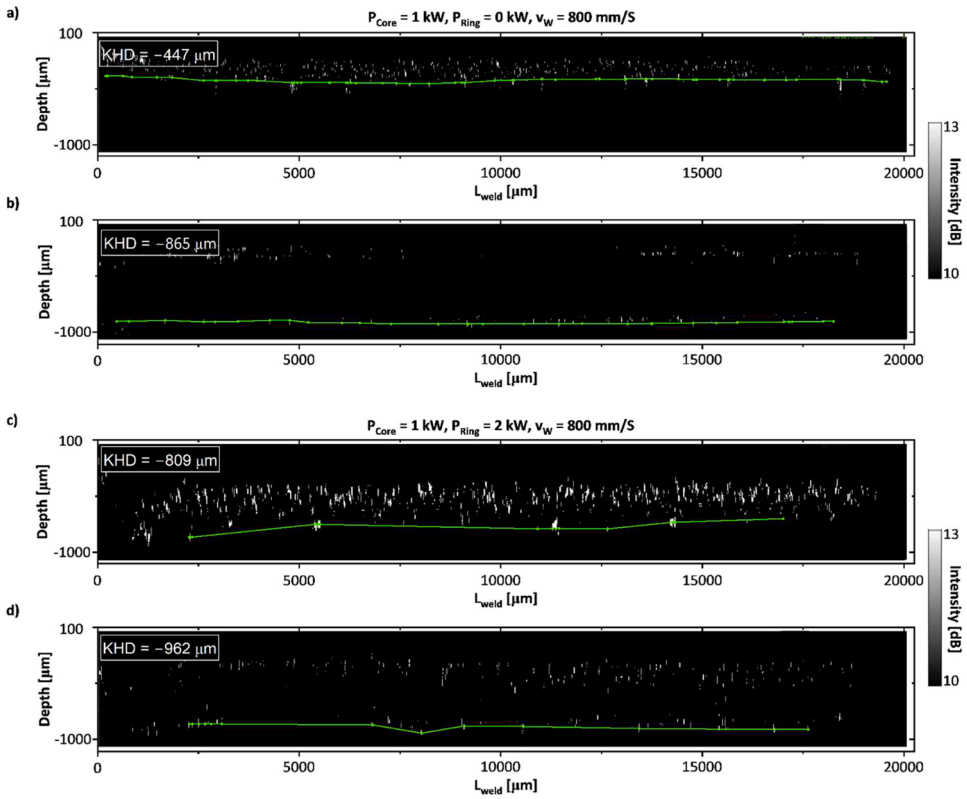

Fig. 11. Resulting OCT depth measurements for: a single-mode core power of 1 kW with no ring power at 800 mm/s after a) a rough calibration and b) a fine calibration; a single-mode core power of 1 kW, a ring power of 2 kW, at 800 mm/s after c) a rough calibration and d) a fine calibration; the green line represents the identified maximum depth profile.

for the ring power, with weld seams shown for $P_{Ring}= 0{\cdot}P_{Core}$ and $P_{Ring}= 2{\cdot}P_{Core}$. In contrast, weld seams for both core powers adopted in this study were illustrated in Fig. 7. The experimental weld depths were further plotted as a function of the different laser process parameters (see Fig. 8). The standard deviations related to the three different sections along the 20 mm weld bead were graphed as well, though not considerable.

It was seen that a restriction of weld speed to lower values yielded in a deeper weld seam profile, directly related to a deeper keyhole. Similar results have been reported in existing welding literature, as the laser energy density interacting with the material welded is inversely proportional to v_w (Xie et al., 2025; M and Steen). For single-mode welds, at $P_{Core}= 1$ kW, varying v_W from 100 mm/s to 800 mm/s led to a decrease in the experimental weld depth from around 1.59 mm to around 0.75 mm. Similarly, the single-mode beam promoted deeper welds as it increased. The center power in core-ring welding applications is majorly responsible for the penetration depth of the weld (Wang et al., 2024; Maina et al., 2018). This is mainly due to its higher intensity, energy density and peak power density, crucial for keyhole promotion and formation. Concerning the ring beam, a considerable enlargement was seen not only from the top of but all over the weld section. The ring power contributed to a widening of the keyhole during the weld process, as it distributes the heat input across a wider area compared to the core beam (Jabar et al., 2023). Overall, the metallographic cross-sections revealed that a high weld speed combined with no ring-power led not only to a shallower but also a narrower keyhole. In addition, it was seen that no pores were formed, which might indicate that the keyhole was not collapsing during the weld (Reinheimer et al., 2025; Matsunawa et al., 2003). Also, no transverse cracks appeared for all of the achieved welds with the different laser sets of parameters.

Iteration counts as a function of process parameters

Fig. 9 displays the iteration counts for a “fine alignment” process with respect to the different laser process parameters. The maximum iteration counts, up until a satisfactory process was reached, were noted when only the core power was present, with an absence of the ring power, and for a weld speed of 800 mm/s. For $P_{Core}= 1$ and 2 kW, the iteration count was 17 and 18, respectively. Those combinations of laser parameters led to the smallest and tightest keyhole, thus implying an even more sensitive OCT alignment. This can be explained by the absence of the annular profile. The single-mode beam, having a spot diameter of only 40 µm, is in the order of magnitude of the OCT focal diameter (34 µm). Whenever it is coupled with a high weld speed, the overall positioning of the OCT beam within the keyhole becomes delicate, hence the high count of iterations. Whereby, as the ring power increased, i.e. from $0{\cdot}P_{Core}$ to $2{\cdot}P_{Core}$, a decrease in the iteration count was noticed. Along with that, a decrease in weld speed led to the same notice. For instance, the iteration count for a $P_{Core}= 1$ kW, a $P_{Ring}= 2$ kW, and a $v_w= 100$ mm/s was only 3.

Regarding the “rough alignment” protocol for the OCT beam position relative to the keyhole a maximum of three iterations was performed for each parameter set. This limitation was maintained in such a consistent manner, across all experimental conditions, to establish a foundation alignment protocol. Subsequently, both results in terms of accuracy and reliability of both the fine and the rough alignment protocols were compared in section "Discussion".

OCT measurement performance

3D keyhole pointcould analysis after a fine alignment

The OCT beam was positioned in the finally obtained x-y coordinates for a “fine alignment” for each process parameter combination. In

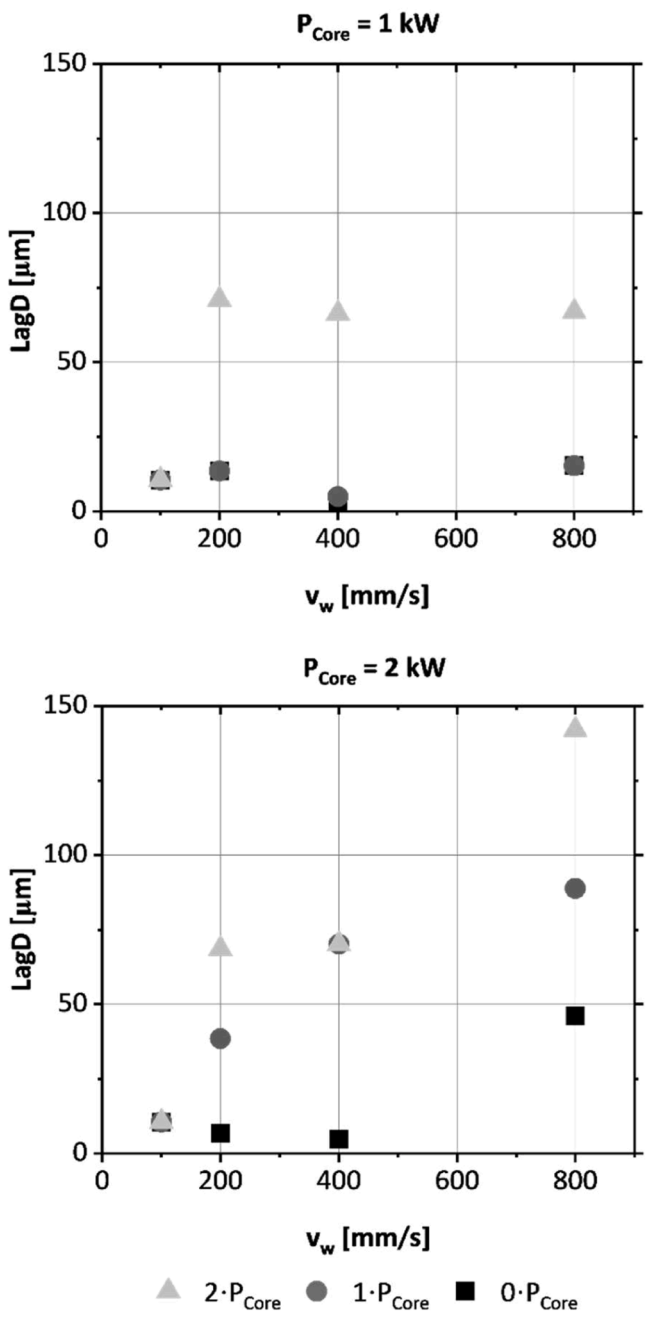

Fig. 12. Influence of the process parameters on the lag distance of the OCT (LagD) with respect to the laser beam for a fine alignment protocol.

general, the regions mapped via the OCT system do not include data at each scan position. These regions where no data is acquired are empty. This loss of fidelity is caused by the scanning technique of the OCT in the 3D View utility (Boley et al., 2018). This measurement sensitivity of the OCT is an inherent disadvantage. Subsequently, and in order to enhance both the completeness and quality of the reconstructed geometry, the dataset of all FOVs were overlapped into a single pointcloud. Such an approach allowed the integration of the coarser information acquired from the top surface of the keyhole, i.e. for higher FOVs, into the finer keyhole local details, i.e. for lower FOVs, thereby improving the analysis of the final 3D representation. Fig. 10 shows the 3D orientations of the data representing the cross-sections shown in Fig. 7.

The 3D pointcloud comprises data of the top surface of the specimen (in relation to a FOV of 2000 × 2000 µm), data of the keyhole's inner walls (in relation to FOV of 1000 × 1000 µm), and data of the keyhole's bottom (in relation to FOV of 500 × 500 µm). The depth of the individual measurements is represented by the color scale. The dimension of an individual datapoint in the 3D pointcloud is not representative of the OCT beam size and is only for visualization. The top surface of the specimen is pre-set at 6000 µm in the positive z-direction. The keyhole wall data and the keyhole bottom data are present below $z = 6000$ µm. Fundamentally, due to the high reflectivity of the Al alloy, the melt pool around the produced keyhole during the weld process results as unstable (Xie et al., 2025). The consequence of the instability can be seen within the returned fluctuating signals of the datapoints above $z = 6000$ µm. Additionally, the noise datapoints lying around the keyhole could be attributed to either fluctuations of the keyhole, or various OCT noise signals, including detector noise, speckle, and autocorrelation (Xie et al., 2023; Boley et al., 2019; Krause et al., 2022). Variations of the keyhole dimensions were similar to the ones of the weld seams illustrated in the metallographic cross-section (see Fig. 7), where a narrower and shallower keyhole resulted with a higher weld speed, coupled with a lower ring beam power.

In-situ keyhole depth measurements

Fig. 11 a and b illustrate OCT acquisitions in the KDM module for welds produced with only the single-mode power of 1 kW, at a weld speed of 800 mm/s, for rough and fine alignments, respectively. This combination of process parameters led to the shallowest and narrowest keyhole observed. The green line represents the tracking algorithm that identifies the maximum depth positions used to monitor the keyhole depth along the weld line, while the white dots represent the returned signals within the OCT detector. Each alignment process was associated with a lag distance, varying with the different set of parameters. For this case, the fine alignment resulted in a lag distance of approximately 15 µm after seventeen iterations, whereas the rough alignment used a lag distance of approximately 100 µm after three iterations. The OCT-based keyhole depth measured at 0.44 mm for rough alignment, and 0.86 mm for fine alignment. The standard deviations associated with the measured keyhole depth were 0.36 mm and 0.17 mm, respectively

In addition, in order to investigate the effect of the ring beam profile, Fig. 11 c and d provide OCT acquisitions for welds with P_{Ring}= 2 kW, at a weld speed v_W= 800 mm/s, again for rough and fine alignments, respectively. In this case, the lag distance that was extracted after a fine alignment was 67 µm with seven iterations. Instead, for the rough alignment, the lag distance was determined to be approximately 170 µm, after three iterations. The OCT-based keyhole depths from the OCT acquisitions were 0.8 mm (rough) and 0.96 mm (fine), with standard deviations of 0.07 mm and 0.03 mm, respectively. In all cases, the OCT keyhole depth was of higher value whenever a fine alignment process was performed, presumably confirming the accuracy of the OCT beam alignment towards the deepest point of the keyhole. Moreover, fine alignment required fewer iterations when the ring beam was present—seventeen iterations using only the single-mode beam versus seven with the ring beam superimposed—indicating an easing of the process and enlarging of the section of the keyhole. In contrast, the rough alignment of the OCT beam led to a considerable underestimation of the keyhole depth. The difference in the measurements obtained highlights the sensitivity of the OCT and emphasizes the importance of precise alignment. Finally, the difference in the measured keyhole depth between a rough alignment and a fine alignment was decreased whenever the ring power was adopted, due to further accessibility of the OCT beam in the deepest region.

Keyhole position

As the keyhole fluctuated during the weld process, and since its shape and volume are dependent on weld parameters (Dorsch et al., 2019), the OCT beam positioning within the keyhole was strategically varied with the variability of P_{Core}, P_{Ring}, and v_W. The lag distance values (LagD) associated with a fine alignment were expected to have been

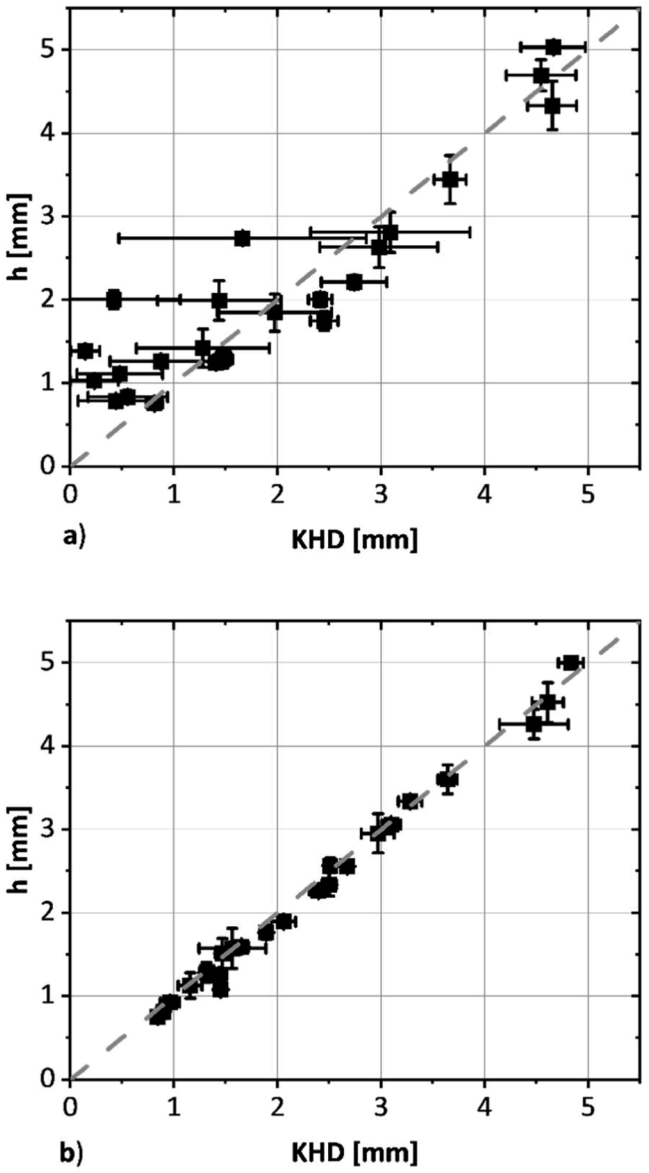

Fig. 13. Comparative analysis between the cross-sectional weld depth h and the keyhole depth obtained from in-situ OCT acquisitions for a) a rough alignment and b) a fine alignment.

positioned accurately towards the deepest point of the keyhole. In contrast, for a rough alignment, and since the iterations were limited, and the keyhole's inner core was not accurately predicted within the 3D View utility, the LagD values associated to this protocol were expected to have been positioned unreliably and in the periphery of the deepest point of the keyhole. For this reason, the values of the lag distance of the OCT beam for only a fine alignment and their variation with respect to the welding parameters are graphed in Fig. 12. The majority of the values of LagD were found to vary between 20 μm and 80 μm, which underlines the sensitivity of the process due to the low order of magnitude of the values. It was noted that an increase in the ring power led to an increase in LagD. In contrast, as the weld speed increased from 100 mm/s to 800 mm/s, LagD showed limited variability, with a slight increase for a P_{Core}= 2 kW. The further increase in weld speed might have moved the keyhole root backwards of the laser beam. The removal of high aspect ratio slightly lagged the keyhole compared to slower weld speeds (Cunningham et al., 2019). Additionally, increasing the core power from 1 kW to 2 kW maintained the lag distances, with minor variations in values.

Discussion

The reliability of the in-situ OCT monitoring process was assessed by directly comparing the acquired keyhole depth KHD to the metallographic cross-sectional weld depth h, for both rough and fine alignments. Standard deviations of the average cross-sectional weld depth h and the KHD monitored alongside the weld length were considered. This comparison, shown in Fig. 13, reveals the noticeable differences in measurement accuracy based on both alignment protocols.

The "rough alignment" protocol resulted in significantly higher standard deviations and greater fluctuations, seen in Fig. 13 a. The dispersion of datapoints is a direct indicator of higher error values, where KHD values did not often match h values. Conversely, an opposite behavior is seen in Fig. 13 b for a "fine alignment", where a strong correlation is present between KHD and h. The error was minimal, coupled with a suppression of fluctuations. The standard deviations for the KHD measurements also noticeably decreased, subsequently indicating a reliable and stable acquisition. These observations strongly link the measurement accuracy to the alignment protocol, as well as the process parameters-dependent keyhole shape and volume, specifically the presence or absence of the ring beam. In addition, to quantify the agreement between the OCT measurements and cross-sectional weld depths, the percentage deviation was computed. Within the "fine alignment" protocol, the deviation remained within approximately 5–15%, whereby significantly larger values were observed for rough alignment. The schematics in Fig. 14 help clarify the underlying concepts of the results.

Laser beam welds performed with only the single-mode beam yielded in a narrower keyhole (Fig. 14 a and b). This explains the higher iterations count (see Fig. 9) required for a "fine alignment". Accurately positioning the OCT beam of approximately 34 μm diameter within the keyhole's deepest point generated by the single-mode beam of ≈ 40 μm diameter is therefore a sensitive task. For these narrow keyholes, an erroneous lag distance frequently resulted with a "rough alignment" (Fig. 14 b). Conversely, the inclusion of the ring profile widened the section of the keyhole (Fig. 14 c and d) and additionally flattened its bottom. This widening eased the alignment process by increasing the accessibility of the OCT beam within the keyhole. This observation is consistent with the lower number of iterations required for alignment when a ring beam was introduced. As a result, the annular profile suppressed the fluctuations between KHD and h, even in cases where the alignment was not perfect. The similar order of magnitude of the laser beam and the OCT beam is the main factor underlining the sensitivity of the process. The probability of positioning the OCT beam far from the keyhole's deepest point stands out when a "rough alignment" protocol is implemented, thus rendering the results inaccurate. The previously highlighted higher deviations support the claim. Whereby, with a "fine alignment" protocol, the keyhole depth was monitored and measured reliably, with lower deviations observed in the results, even for the narrowest and shallowest keyholes. It should be noted that in some cases, the measured KHD was found to be slightly higher than h. This may be due to the multiple reflections phenomena of the OCT beam within the keyhole during the in-situ acquisitions, which may have played a noticeable role in the case of small-shaped keyholes (Boley et al., 2018).

The high reliability of the "fine alignment" in this study is supported by the absence of pores in the metallographic cross-sections. As represented in the schematic of Fig. 14 e, keyhole tilting and bulging are

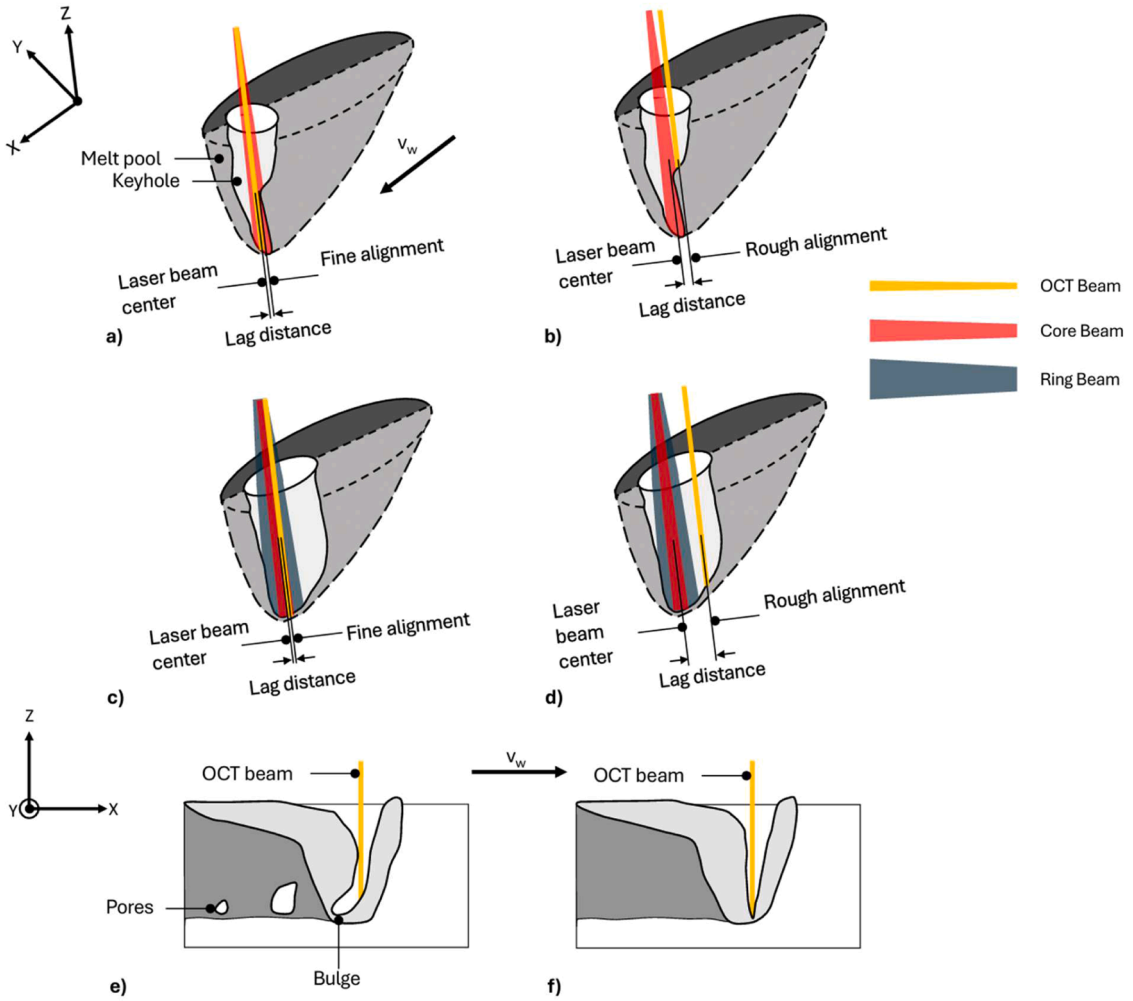

Fig. 14. Representative sketches of a) and c) a fine alignment and b) and d) a rough alignment, for a) and b) a single-mode core beam laser weld and c) and d) a single-mode core and ring beams laser weld, e) a tilting keyhole, and f) a non-tilting keyhole.

mechanisms linked to pore formation during the weld (Matsunawa et al., 2003; Florian et al., 2025). The same geometrical behavior would limit the OCT beam's accessibility to the keyhole's deepest point, in that case well behind its opening, causing multiple reflections off the keyhole walls. Instead, with the consistent absence of pores observed in the cross-sections, a possible non-tilting keyhole might have been produced (Fig. 14 f), even at higher weld speeds. This stable-resulting geometry of the keyhole is considered an ideal condition for the OCT beam, allowing the measuring beam to be positioned accurately and measure the keyhole's true depth. In general, in case of tilting keyholes, a "fine alignment" protocol alone would not be enough to obtain reliable results, as the process might suffer from multiple reflections of the OCT beam inside the keyhole. The measurements would directly lead to higher values compared to the cross-sectional weld depth, and even possible loss of signal quality. To mitigate this problem, an increase in the ring power as a means to enlarge the keyhole's section and suppress its backwards tilting can be done. Furthermore, it has been shown in literature that launching the OCT beam to the keyhole's top opening with a certain incident angle can decrease the measurement error and improve the quality of the signal overall. When the OCT beam is already aimed past the front wall of the keyhole and into its back wall, the tilting is anticipated, and the multiple reflection phenomena can be suppressed (Schmoeller et al., 2019).

Conclusions

This paper presented a systematic methodology for calibrating and validating in-situ keyhole depth (KHD) measurements using optical coherence tomography (OCT) with novel beam shaping technologies, consisting of a single-mode core beam coupled with a coaxial ring beam. The core focus of the study centered on comprehending the sensitivity of the OCT in-situ acquisitions of the KHD with respect to its alignment within the keyhole, as well as to adoption of different beam shaping configurations.

Central to this study was a definition of an iterative approach to position the OCT beam within the keyhole during the weld based on a lag distance, essential for the comprehension of the sensitive nature of the OCT alignment. Two alignment protocols, namely the "fine alignment" and the "rough alignment" protocols, were developed. A direct comparison between the first (up to 18 iterations) and the second (up to 3 iterations) was conducted. The "rough alignment" protocol resulted in a significant underestimation of the KHD, coupled with a high signal variance and poor correlation with the cross-sectional weld depth h. Conversely, the "fine alignment" protocol, with a more precise positioning of the OCT beam within the keyhole's deepest point, yielded in a minimal error difference between KHD and h, underlining a more reliable acquisition. The sensitivity of the OCT calibration process could be

expanded beyond the iterative process, and to the systematic effect of novel beam shaping technologies. Welds applied with only the single-mode beam showed a noticeable challenge within the OCT alignment process due to its comparable diameter with that of the OCT beam. This was most evident with welds with weld speeds of up to 800 mm/s, which produced the narrowest and shallowest keyhole shapes and required the highest number of iterations (up to 18) for accurate acquisitions. Whereby, the addition of coaxial ring power led to a widening of the keyhole's section and a flattening of its bottom. This geometric change had a direct effect on the alignment protocol, easing the spatial positioning of the OCT beam, with respect to the laser beam, and decreasing the required number of iterations for reliable acquisitions.

In view of the multiple iterations in its current manual implementation, future investigations aim to automate the process. In industrial processes, this can be accelerated through the development of a closed-loop system that can automatically identify the keyhole's deepest point coordinates with respect to the laser beam and lock the OCT onto it would mitigate the limitations of the approach, leading to an industrial-scale adoption of the technique.

CRediT authorship contribution statement

Serge André Dib: Writing – review & editing, Writing – original draft, Visualization, Validation, Methodology, Investigation, Formal analysis, Data curation, Conceptualization. **Ali Gökhan Demir:** Writing – review & editing, Validation, Supervision, Project administration, Methodology, Conceptualization.

Declaration of competing interest

The authors declare that they have no known competing financial interests or personal relationships that could have appeared to influence the work reported in this paper.

Acknowledgements

The authors gratefully acknowledge BLM Group for the longstanding collaboration. MKS Ophir is acknowledged for the support provided during the beam profile measurements.

Data availability

Data will be made available on request.

References

A.G. Demir et al., Challenges and opportunities for laser applications in electric vehicle manufacturing, vol. Part F1351. 2024. doi: 10.1007/978-3-031-41163-2_12.

Beck, T., Bantel, C., Boley, M., Bergmann, J.P., 2021. Oct capillary depth measurement in copper micro welding using green lasers. Appl. Sci. 11 (6). https://doi.org/10.3390/app11062655.

Blug, A., et al., 2011. Closed-loop control of laser power using the full penetration hole image feature in aluminum welding processes. Phys. Procedia 12, 720–729. https://doi.org/10.1016/j.phpro.2011.03.090.

Boley, M., et al., 2013. Investigating the weld depth behaviour using different observation techniques: x-ray, inline coherent imageing and highspeed observation during welding ice. In: ICALEO 2013 - 32nd Int. Congr. Appl. Lasers Electro-Optics, no. Ici, pp. 22–27. https://doi.org/10.2351/1.5062880.

Boley, M., Fetzer, F., Weber, R., Graf, T., 2019. Statistical evaluation method to determine the laser welding depth by optical coherence tomography. Opt. Lasers Eng. 119, 56–64. https://doi.org/10.1016/j.optlaseng.2019.03.014. December 2018.

Boley, M., Webster, P., Heider, A., Weber, R., Graf, T., 2018. Investigating the Keyhole Behavior By Using X-Ray and Optical Depth Measurement Techniques. Ldd, pp. 426–430. https://doi.org/10.2351/1.5063091.

Dupriez, N.D., Denkl, A., 2017. Advances of OCT technology for laser beam processing. Laser Tech. J. 14 (4), 34–38. https://doi.org/10.1002/latj.201700021.

F. Dorsch, T. Harrer, P. Haug, and S. Plasswich, "Process control using capillary depth measurement," vol. 1505, p. 1505, 2019, doi: 10.2351/1.5118550.

Fleming, T.G., et al., 2023. Synchrotron validation of inline coherent imaging for tracking laser keyhole depth. Addit. Manuf. 77, 103798. https://doi.org/10.1016/j.addma.2023.103798. April.

Florian, T., et al., 2025. Combining in situ synchrotron X-ray imaging and multiphysics simulation to reveal pore formation dynamics in laser welding of copper. Int. J. Mach. Tools Manuf. 204, 104224. https://doi.org/10.1016/j.ijmachtools.2024.104224. February 2024.

Galbusera, F., Caprio, L., Previtali, B., Demir, A.G., 2024. Analytical modeling and characterization of ring beam profiles for high-power lasers used in industrial manufacturing. J. Manuf. Process. 117, 387–404. https://doi.org/10.1016/j.jmapro.2024.02.069. February.

Haeusler, A., Hollatz, S., Olowinsky, A., Gillner, A., Poprawe, R., 2018. Quality improvement of the surface of laser micro welds by using a dual beam setup. J. Laser Appl. 30 (3). https://doi.org/10.2351/1.5040626.

He, G., Gao, X., Li, L., Gao, P., 2024. OCT monitoring data processing method of laser deep penetration welding based on HDBSCAN. Opt. Laser Technol. 179, 111303. https://doi.org/10.1016/j.optlastec.2024.111303. March.

Hollatz, S., Hummel, M., Jaklen, L., Lipnicki, W., Olowinsky, A., Gillner, A., 2020. Processing of keyhole depth measurement data during laser beam micro welding. Proc. Inst. Mech. Eng. Part L J. Mater. Des. Appl. 234 (5), 722–731. https://doi.org/10.1177/1464420720916759.

Huegel, H., Graf, T., 2009. Laser in Der Fertigung. Vieweg + Teubner, Wiesbaden.

Jabar, S., Baghbani Barenji, A., Franciosa, P., Kotadia, H.R., Ceglarek, D., 2023. Effects of the adjustable ring-mode laser on intermetallic formation and mechanical properties of steel to aluminium laser welded lap joints. Mater. Des. 227, 111774. https://doi.org/10.1016/j.matdes.2023.111774.

M. Kogel-Hollacher, M. Schoenleber, T. Bautze, M. Strebel, and R. Moser, "Measurement and closed-loop control of the penetration depth in laser materials processing," 2016.

Köhler, T., Raab, M., Regensburg, A., Bergmann, J.P., 2019. Liquid Interlayer Formation During Torsional Ultrasonic Welding of EN CW004A and EN AW1050. Weld. World, pp. 1187–1194. https://doi.org/10.1007/s40194-019-00763-8.

Krause, T.J.H., Allen, T.R., Fraser, J.M., 2022. Self-witnessing coherent imaging for artifact removal and noise filtering. Opt. Lasers Eng. 151, 106936. https://doi.org/10.1016/j.optlaseng.2021.106936. March 2021.

Maina, M.R., Okamoto, Y., Okada, A., Närhi, M., Kangastupa, J., Vihinen, J., 2018. High surface quality welding of aluminum using adjustable ring-mode fiber laser. J. Mater. Process. Technol. 258 (December 2017), 180–188. https://doi.org/10.1016/j.jmatprotec.2018.03.030.

Matsunawa, A., Mizutani, M., Katayama, S., Seto, N., 2003. Porosity formation mechanism and its prevention in laser welding. Weld. Int. 17 (6), 431–437. https://doi.org/10.1533/wint.2003.3138.

Maurya, A.K., Khan, W.N., Patnaik, A., Adin, M.Ş., Chhibber, R., Pandey, C., 2024. Tribological performance of gas tungsten arc welded dissimilar joint of sDSS 2507/IN-625 for marine application. Arch. Civ. Mech. Eng. 24 (1), 1–15. https://doi.org/10.1007/s43452-023-00832-2.

Mittelstädt, C., Mattulat, T., Seefeld, T., Kogel-Hollacher, M., 2019. Novel approach for weld depth determination using optical coherence tomography measurement in laser deep penetration welding of aluminum and steel. J. Laser Appl. 31 (2). https://doi.org/10.2351/1.5082263.

M. Schmoeller, T. Weiss, K. Goetz, C. Stadter, M.F. Zaeh, and C. Bernauer, "Keyhole depth measurement and fuzzy control," 2022.

Mohammadzadeh Sanandaji, M., Mollick, R., Ratner, A., Ding, H., 2025. Laser-enabled organic coating for sustainable PFAS-free metal surfaces. Manuf. Lett. 45, 8–12. https://doi.org/10.1016/j.mfglet.2025.06.198.

"P. James and L. Webster, 'Inline Coherent Imaging', 2012.".

R. Cunningham et al., "Keyhole threshold and morphology in laser melting revealed by ultrahigh-speed x-ray imaging," vol. 363, no. 6429, pp. 849–852, 2019, doi: 10.1126/science.aav4687.

Reinheimer, E.N., et al., 2025. Avoiding the formation of pores during laser welding of copper hairpins by dynamic beam shaping. Int. J. Adv. Manuf. Technol. 137 (5), 2257–2266. https://doi.org/10.1007/s00170-025-15236-0.

Schmoeller, M., Stadter, C., Liebl, S., Zaeh, M.F., 2019. Inline weld depth measurement for high brilliance laser beam sources using optical coherence tomography. J. Laser Appl. 31 (2). https://doi.org/10.2351/1.5096104.

Schmoeller, M., Stadter, C., Wagner, M., Zaeh, M.F., 2020. Investigation of the influences of the process parameters on the weld depth in laser beam welding of AA6082 using machine learning methods. Procedia CIRP 94, 702–707. https://doi.org/10.1016/j.procir.2020.09.121. March.

Shu, L., Ma, D., Cao, S., Wang, Y., Jiang, P., Geng, S., 2025. Optical coherence measurement-based penetration depth monitoring of stainless steel sheets in laser lap welding using long short-term memory network. Opt. Laser Technol. 181, 111811. https://doi.org/10.1016/j.optlastec.2024.111811. PB.

Sokolov, M., et al., 2021. Applying optical coherence tomography for weld depth monitoring in remote laser welding of automotive battery tab connectors. J. Laser Appl. 33 (1). https://doi.org/10.2351/7.0000336.

Spurk, C., Hollatz, S., Lipnicki, W., Hummel, M., Gillner, A., Häfner, C., 2024. Controlling the weld penetration depth of laser beam micro welding by using an iterative learning approach. Materwiss. Werksttech. 55 (4), 533–543. https://doi.org/10.1002/mawe.202300154.

"W. M. and M.J. Steen, Laser Material Processing. Springer Science & Business Media.".
Wang, L., et al., 2020. Monitoring of keyhole entrance and molten pool with quality analysis during adjustable ring mode laser welding. Appl. Opt. 59 (6), 1576. https://doi.org/10.1364/ao.383232.
Wang, Z., et al., 2024. Mitigating spatters in keyhole-mode laser welding by superimposing additional ring-shaped beam. Opt. Laser Technol. 168, 109869. https://doi.org/10.1016/j.optlastec.2023.109869. August 2023.
Webster, P.J.L., Leung, B.Y.C., Yu, J.X.Z., Anderson, M.D., Hoult, T.P., Fraser, J.M., 2010. Coaxial real-time metrology and gas assisted laser micromachining: process development, stochastic behavior, and feedback control. Micromach. Microfabr. Process Technol. XV 7590, 759003. https://doi.org/10.1117/12.842409.
Xie, G., et al., 2023. An efficient method for laser welding depth determination using optical coherence tomography. Sensors 23 (11). https://doi.org/10.3390/s23115223.
Xie, G., et al., 2025. Keyhole morphology monitoring in laser welding using optical coherence tomography. Chinese Opt. Lett. 23 (3), 031201. https://doi.org/10.3788/col202523.031201.